

The Intrabinary Shock and Companion Star of Redback Pulsar J2215+5135

ANDREW G. SULLIVAN ¹ AND ROGER W. ROMANI ¹

¹*Kavli Institute for Particle Astrophysics and Cosmology, Department of Physics, Stanford University, Stanford, CA 94305, USA*

ABSTRACT

PSR J2215+5135 (J2215) is a ‘redback’ spider pulsar, where the intrabinary shock (IBS) wraps around the pulsar rather than the stellar-mass companion. Spider orbital light curves are modulated, dominated by their binary companion thermal emission in the optical bands and by IBS synchrotron emission in the X-rays. We report on new *XMM*-Newton X-ray and U-band observations of J2215. We produce orbital light curves and use them to model the system properties. Our best-fit optical light model gives a neutron star mass $M_{NS} = 1.98 \pm 0.08 M_{\odot}$, lower than previously reported. However, uncertainty in the stellar atmosphere metallicity, a parameter to which J2215 is unusually sensitive, requires us to consider an acceptable systematic plus statistical range of $M_{NS} \sim 1.85 - 2.3 M_{\odot}$. From the X-ray analysis, we find that the IBS wraps around the pulsar, but with a pulsar wind to companion wind momentum ratio unusually close to unity, implying a flatter IBS geometry than seen in other spiders. Estimating the companion wind momentum and speed from the X-ray light curve, we find a companion mass-loss rate of $\dot{M}_c \gtrsim 10^{-10} M_{\odot} \text{ yr}^{-1}$, so that J2215 may become an isolated millisecond pulsar in ~ 1 Gyr. Our X-ray analyses place constraints on the magnetization and particle density of the pulsar wind and support models of magnetic reconnection and particle acceleration in the highly magnetized relativistic IBS.

Keywords: Pulsars (1306) – Binary pulsars (153)

1. INTRODUCTION

Spider pulsars found in compact binaries with a low-mass companion star have orbital periods $P_b \lesssim 1$ day. The companion mass determines whether the spider falls into the black widow ($M_c < 0.1 M_{\odot}$) or redback ($M_c \approx 0.1 - 0.4 M_{\odot}$) category. In these systems, pulsar gamma-ray emission and the relativistic particles from the pulsar wind irradiate the companion, consequently driving off a massive stellar wind (Kluźniak et al. 1988; van Paradijs et al. 1988; Roberts 2013; Hui & Li 2019). The pulsar wind and companion wind collide to form an intrabinary shock (IBS). In redbacks which typically have higher stellar wind momentum fluxes, the companion wind dominates the pulsar wind so the IBS wraps around the pulsar, while in black widows with lower stellar wind momentum fluxes, the IBS wraps around the companion, as the pulsar wind dominates the stellar wind (Romani & Sanchez 2016; Wadiasingh et al. 2017; Kandel et al. 2019).

X-ray observations may probe the IBS while optical observations typically reveal the companion heating. Particles in the shocked pulsar wind accelerate and emit synchrotron X-rays (Kandel et al. 2019, 2021). The light

curves are characterized by two caustic peaks per orbital phase, associated with the beamed emission from relativistic particles traveling tangent to the observing line of sight. Thermal emission from the companion is generally boosted by reprocessed pulsar gamma-rays on the ‘day’ side of the companion and sometimes by precipitating IBS particles reprocessed in surface hot spots. Consequently, X-ray light curve and spectral analyses reveal the IBS structure and particle acceleration mechanisms, while optical analyses examine heating of the companion surface.

PSR J2215+5135 (J2215 hereafter) is a redback millisecond pulsar (MSP) with spin period $P_s = 2.61$ ms and spin-down power $\dot{E} = 5 \times 10^{34} I_{45} \text{ erg s}^{-1}$ in a $P_b = 4.14$ hr orbit with a $M \approx 0.3 M_{\odot}$ companion (Hessels et al. 2011). The source has dispersion measure of 69.2 pc cm^{-3} (Hessels et al. 2011), which corresponds to an estimated distance ~ 3 kpc (Yao et al. 2017, e.g.). First detected as an unidentified gamma-ray source by the *Fermi* Large Area Telescope (*Fermi*-LAT) (Atwood et al. 2009) and discovered by 350 MHz Green Bank Telescope followup observations (Ray et al. 2012; Hessels et al. 2011), J2215 has been studied optically (Breton et al. 2013; Schroeder & Halpern 2014; Romani et al.

2015; Linares et al. 2018), in radio (Hessels et al. 2011; Broderick et al. 2016), in gamma-rays (Romani et al. 2015), and briefly in X-rays (Gentile et al. 2014; Linares 2014) prior to this work.

Earlier optical light curve modeling suggests that J2215 contains a particularly massive neutron star $\gtrsim 2 M_{\odot}$ (Linares et al. 2018; Kandel & Romani 2020, hereafter KR20). KR20 estimate a neutron star mass of $M_{NS} = 2.24 \pm 0.09 M_{\odot}$ using a companion surface optical model that contains a magnetic pole hot spot. Such a massive neutron star would constrain properties of the dense matter equation of state (Lattimer & Prakash 2007; Steiner et al. 2013; Brandes et al. 2023). Previous modeling is sensitive to the poorly constrained companion hot spot, adding uncertainty to the binary inclination i and, by extension, M_{NS} estimates. Unusually, the previous best-fit companion model has sub-solar metallicity with $\log Z = -1$. Also, older X-ray observations, which suggested widely separated light curve peaks and a flat IBS, relied on an *XMM-Newton* exposure with strong background flaring and only two binary orbits. Thus, we conduct more detailed optical and X-ray study to better understand the robustness and systematics of the companion heating model and probe the IBS physics.

In this paper, we present the results of light curve analyses of new *XMM-Newton* J2215 X-ray and U band observations. In sec. 2, we summarize the new data, presenting the X-ray and U light curves. In sec. 3, we discuss our analysis of the collected X-ray spectra. In sec. 4, we show the results of optical companion heating and X-ray IBS light curve analyses. We discuss our results and their implications in sec. 5.

2. XMM-NEWTON OBSERVATIONS

The *XMM-Newton* Observatory (Jansen et al. 2001) performed three new observations of J2215, the first two on 2022 June 8-11 (ObsIDs 0900770101 and 0900770201) and the third on 2022 December 1 (ObsID 0900770301) lasting a total of 120.7 ks. These observations provided both X-ray and U band data, which are presented here for the first time. We supplement these new observations with an archival 54.9 ks *XMM-Newton* X-ray observation (ObsID 0783530301). We perform data reduction using tools of the *XMM-Newton* Scientific Analysis System (SAS) (Jansen et al. 2001).

2.1. X-rays

We process the EPIC-PN (PN) and EPIC-MOS (MOS) X-ray data using the SAS tools *eproc* and *emproc*. We perform standard barycenter corrections using the SAS *barycen* tool and filter out background flaring

events. After this processing, the total exposure times for PN and the MOS cameras are 100.9 ks and 128.5 ks across 14 orbits. We extract the source from a circular region with radius $\sim 30''$ and select circular background regions on the same detector chip as the source with radii 4-5 times larger than the source aperture. We obtain background subtracted X-ray light curves for the three detectors from the SAS tool *epicccorr*.

For the orbital parameters, we use the *Fermi*-LAT third gamma-ray pulsar catalog ephemeris valid from 2008 August 4 until 2019 December 22 for all observations (Smith et al. 2023), as this is the most recent published ephemeris for J2215. The times of ascending node (TASC) deviate from the mean by less than 0.003 in phase for the entire ephemeris range, so we expect no significant shift in the TASC at our epoch (although 1.5-2 yr outside the ephemeris range). The observed phase of the Optical Monitor (OM) U light curve, to be discussed in the following subsection, is in good agreement with the ephemeris prediction.

We convert the PN and MOS light curves from count rate and count rate error to flux in each detector. We combine the data and distribute it into 26 phase bins. We compute the average flux weighted by the inverse square of the errors in each bin. Flux errors are estimated by the standard error of a variance-weighted sample. Our combined 0.5-10 keV X-ray light curve is shown in the top panel of Fig. 1.

2.2. Optical

Contemporaneous OM U filter data was taken in both image and fast mode. The fast mode $10'' \times 10''$ images were obtained from a series of exposures over each observation. We use the SAS tool *omfchain* to obtain U filter light curves. For each exposure, we extract the source from a circular aperture with a radius of 3 detector pixels in the fast mode image and determine the background from the average count rate of the corresponding image mode image with all point sources removed. The extracted count rates are subsequently corrected by the fraction of the point-spread function (PSF) contained in the aperture. After processing, the OM exposure time is 85 ks. We convert the OM U data to flux using the published OM U calibration for A-type stars. We place the data into flux bins by computing the sample mean and standard error. We also use the *Fermi*-LAT third gamma-ray pulsar catalog ephemeris for the orbital parameters. The OM U light curve is shown in the bottom panel of Fig. 1.

3. SPECTRAL ANALYSIS

We divide our X-ray light curve into four phase intervals as labeled in Fig. 1 and perform spectral anal-

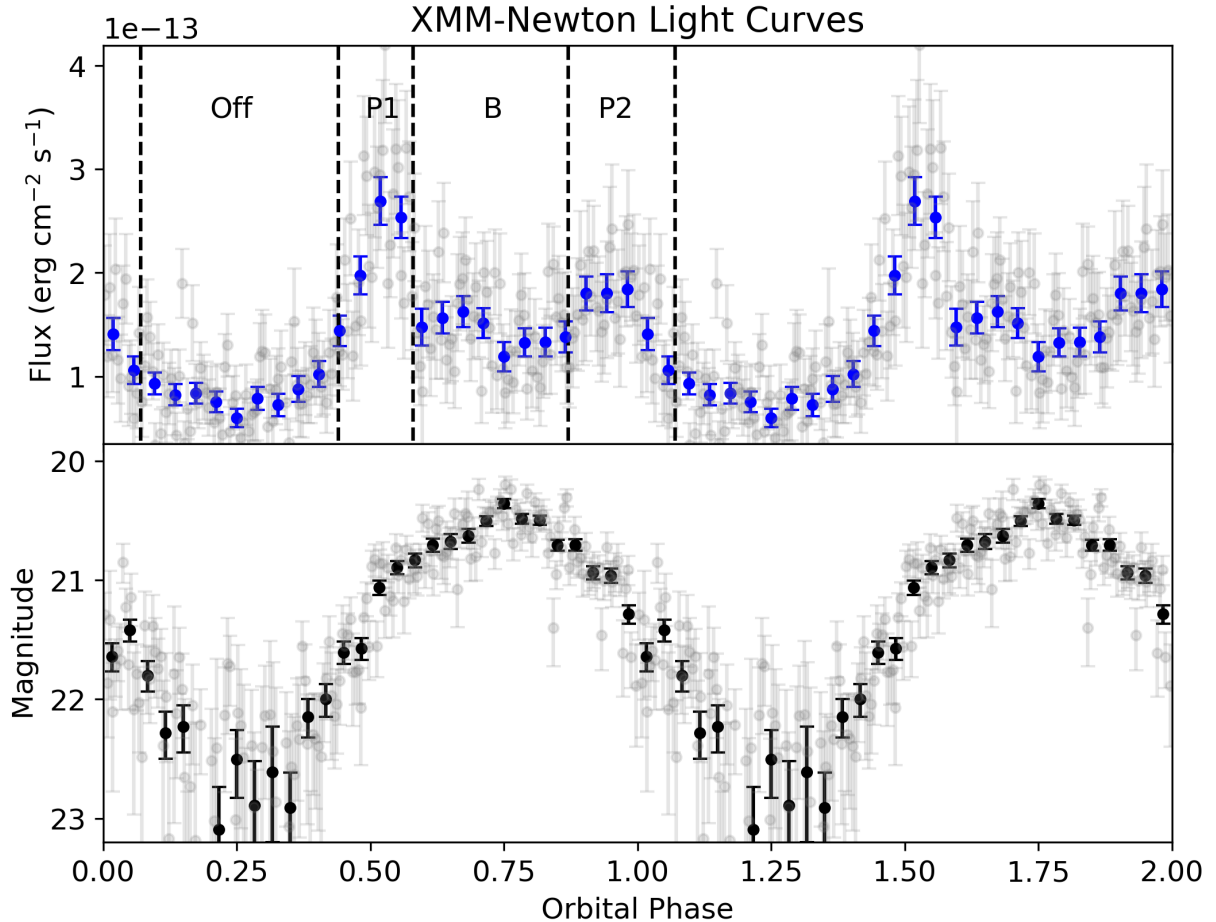


Figure 1. Binned X-ray and optical orbital light curves of J2215. More-finely binned light curves are shown by faded markers. (Top) The combined PN and MOS 0.5-10 keV X-ray light curve. We identify four distinct regions for which we separately fit spectra: two peaks, P1 and P2 corresponding to the two phase intervals in which the flow of the IBS shock is tangent to our line of sight, a bridge (B) between the two peaks, and an off region around the companion inferior conjunction where the X-ray emission comes principally from the IBS nose. (Bottom) The OM U filter light curve for J2215 from the new *XMM-Newton* observations.

yses of these phase bins. We identify Peak 1 (P1; $0.44 < \Phi < 0.58$) and Peak 2 (P2; $0.87 < \Phi < 1.07$) as the two characteristic IBS X-ray peaks (Romani & Sanchez 2016; Kandel et al. 2019). We demarcate a bridge region (B; $0.58 < \Phi < 0.87$) between P1 and P2 and an off region ($0.07 < \Phi < 0.44$) corresponding to the companion at inferior conjunction. Here non-IBS fluxes (e.g. from the magnetosphere or a pulsar wind nebula) may dominate, as only weakly beamed X-rays from the IBS nose are expected. We use the CIAO tool *Sherpa* (Freeman et al. 2001; Doe et al. 2007) to fit non-thermal power-law spectral models to the *XMM* data with spectral indices Γ_{P1} , Γ_{P2} , and Γ_B . We include an additional phase-independent power-law component throughout the orbit with power-law index Γ_0 to account for phase-independent emission. The spectral model in

counts $\text{s}^{-1} \text{cm}^{-2} \text{keV}^{-1}$ in each phase region is

$$f_r(E) = e^{-N_H \sigma(E)} (K_r E^{-\Gamma_r} + K_0 E^{-\Gamma_0}), \quad (1)$$

where N_H is the equivalent hydrogen column, $\sigma(E)$ is the photo-electric cross section, K_r and K_0 are power-law normalization factors, and $r = \{P1, P2, B, Off\}$ demarcates the orbital phase region. For our absorption model, we employ the photoelectric cross sections of Balucinska-Church & McCammon (1992) and the elemental abundances of Anders & Grevesse (1989). In the off phase, $K_r = 0$. The results of our fit are shown in Table 1. Because the spectral indices of P1, P2, and B are not significantly different, we also give the average spectral index across the IBS Γ_{IBS} . Fig. 2 shows the spectra across the IBS as well as in the off phases as observed by PN.

4. LIGHT CURVE MODELLING

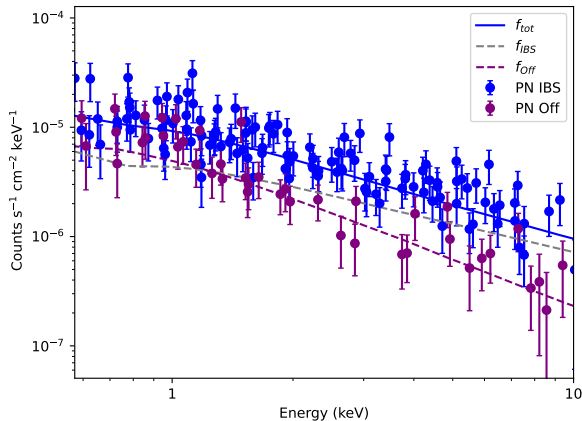


Figure 2. The observed PN X-ray spectra with the equivalent hydrogen column N_H fixed at $0.09 \times 10^{22} \text{ cm}^{-2}$. The plotted points are the spectra in the IBS phase region ($0.44 < \Phi < 1.07$; including P1, P2, and B) as well as in the off region ($0.07 < \Phi < 0.44$). The solid line shows the full model in the IBS phases f_{tot} and the two dashed lines show the absorbed power-law models for the IBS component f_{IBS} with power-law index Γ_{IBS} and the phase-independent component f_{off} with power-law index Γ_0 . Note that in the off region, the only model component is the absorbed power-law f_{off} .

	Fixed N_H	Free N_H
N_H (10^{22} cm^{-2})	0.09	0.10 ± 0.02
Γ_{P1}	0.99 ± 0.11	1.00 ± 0.11
Γ_{P2}	0.85 ± 0.12	0.86 ± 0.12
Γ_B	0.85 ± 0.15	0.86 ± 0.12
Γ_{IBS}	0.94 ± 0.08	0.96 ± 0.08
Γ_0	1.43 ± 0.08	1.48 ± 0.12
F_{tot} ($10^{-14} \text{ erg cm}^{-2} \text{ s}^{-1}$)	15.1 ± 1.6	15.2 ± 1.9
F_{IBS} ($10^{-14} \text{ erg cm}^{-2} \text{ s}^{-1}$)	9.9 ± 1.6	10.0 ± 1.8
F_0 ($10^{-14} \text{ erg cm}^{-2} \text{ s}^{-1}$)	5.3 ± 0.6	5.2 ± 1.0
χ^2/DoF	1.03	1.03

Table 1. X-ray spectral model fits. We fit a phase-independent power-law with index Γ_0 throughout the orbit and add additional power-laws with separate spectral indices in the P1, P2, and B phase regions. The total measured flux in the IBS phase region $0.44 < \Phi < 1.07$ is F_{tot} . The measured flux of the specific IBS component is F_{IBS} , while the phase-independent component is F_0 . The equivalent hydrogen column N_H is fixed at $0.09 \times 10^{22} \text{ cm}^{-2}$, the value inferred from 3D dust maps (Green et al. 2018), in the left column, while allowed to vary in the right.

4.1. Optical Models

Previous optical modeling of J2215 has been conducted by Linares et al. (2018) and KR20 using g'r'i' data from two observing nights at the William Her-

schel Telescope (WHT). These light curve analyses show strong heating asymmetries on the companion star, suggesting the presence of a hot spot, which could plausibly be a magnetic pole (Sanchez & Romani 2017). KR20 include a hot spot at the coordinates (θ_{HS}, ϕ_{HS}) defined from the nose on the stellar surface. At that location, the stellar temperature increases by a factor $(1 + A_{HS})$ from $T \approx 5600 \text{ K}$ to $T \gtrsim 8000 \text{ K}$ with a Gaussian profile over radius r_{HS} . Their best-fit model gives $i = 68.9^\circ$ and consequently a very high $M_{NS} = 2.24 M_\odot$. These results, however, are sensitive to the hot spot parameters. Additionally, they were obtained using a simplified gravity darkening model, which does not account for the gravity darkening of the reprocessed pulsar heating luminosity (Claret & Bloemen 2011; Kandel & Romani 2023).

We refit the WHT g'r'i' data along with the new OM U data using the ICARUS light curve modeling code (Breton et al. 2013) including the extensions described in KR20 and the revised gravity darkening law described in Kandel & Romani (2023). The model is very similar to the best-fit hot spot model of KR20; we augment a direct pulsar heating model with a surface hot spot and add a flat spectrum veiling flux f_2 to the WHT night 2 data. We adopt an extinction $A_V = 0.4$ in these fits, as this matches the fit N_H (Table 1) and is consistent with estimates from current 3-D dust maps (Green et al. 2018). We perform Monte Carlo sampling of the parameters using the library PyMultinest (Feroz & Hobson 2008; Feroz et al. 2009; Buchner et al. 2014; Feroz et al. 2019), which uses nested sampling to search the parameter space. To predict the flux in each photometric band, we use BT-Settl model atmospheres (Allard 2014) available from the Spanish Virtual Observatory (<http://svo2.cab.inta-csic.es>). These model atmosphere spectra are available with a range of metallicities. We have explored models with $\log Z = -1.5$ to $+0.5$; a few models are also available with varying degrees of α process abundance enhancement.

Our fits prefer calibration offsets $\delta m_r \gtrsim 0.03$ to both nights in the WHT r' band and $\delta m_U \approx 0.5$ to the OM U data. We have attempted to find the origin of this large U offset. As noted in Sec. 2.2, we obtain the OM U AB magnitudes by converting from count rate to flux with the SAS-recommended U conversion factor of $1.7 \times 10^{-16} \text{ erg cm}^{-2} \text{ \AA}^{-1} \text{ count}^{-1}$ for A stars. This spectral type is appropriate for the companion near optical maximum. Using archival XMM OM U exposures in fields covered by the Sloan Digital Sky Survey (SDSS), where catalog u magnitudes are available, we have also investigated the calibration manually. We extracted the count rates in 3-pixel apertures centered on bright stars in two SDSS

fields, subtracted the average backgrounds in the images, and scaled the stars' count rates by the calibration aperture correction factor given by SAS. From these data we find a conversion to SDSS u of $2.7 \pm 0.2 \times 10^{-16}$ erg cm $^{-2}$ Å $^{-1}$ count $^{-1}$, which would suggest that the U fluxes are brighter by a factor of ~ 1.6 (or offset by ~ 0.5 mag) with respect to the our XMM calibrated flux, comparable to the fit offset.

We have also examined the calibrated 2014 Keck LRIS spectra of Romani et al. (2015), whose g'r'i colors are consistent with the 2014 WHT photometry. We find the Keck fluxes at wavelengths below 4000 Å are consistent with the family of BT-Settl model atmosphere spectra (Allard 2014) at the day side temperature of the star. A change to the thermal companion flux (unlike the IBS non-thermal flux) seems unlikely and would require a concomitant change in the heating power. Our X-ray flux is consistent with past values and there is no significant change to the (dominant) *Fermi*-LAT gamma-ray heating. Consequently, we consider a U calibration offset the most likely explanation. While fitting for δm_U slightly decreases the predictive power of our model, the OM U light curve shape still probes the hot spot geometry.

When fitting the g'r'i light curve data without including U , we find that the best-fit parameters for i and the hot spot are, unusually, sensitive to the metallicity of the companion stellar atmosphere. This happens for J2215 because the location of the hot spot allows it to mimic a substantial portion of the companion nose heating under the corrected gravity darkening law. With only g'r'i colors, the spot location and temperature are not independently constrained, so there is substantial covariance with i in the fits. Consequently, the subtle metallicity-dependent color differences shift the best-fit i and hot spot parameters. For each atmosphere model, we show the $\Delta\chi^2$ from the best fitting metallicity model as well as the estimated inclination in Fig. 3. This hot spot metallicity sensitivity seems to be a peculiarity of J2215's parameters; we do not see such sensitivity in our fits of other objects (Draghis et al. 2019). Nevertheless, this remains a possible rare systematic that should be checked in spider model fitting.

The enhancement of α -process elements increases as $\log Z$ decreases in the BT-Settl models. For $\log Z \geq 0$, all models have $\alpha = 0$, while for $\log Z \leq -1$ the bulk of the models have $\alpha = 0.4$. At $\log Z = -0.5$ most models have $\alpha = 0.2$, but there are a subset at $\alpha = 0$ that span fewer temperatures and surface gravity values. With the WHT g'r'i data, we find that super-solar metallicities are unacceptable while all $\log Z \leq 0$ give comparable χ^2 (see Fig. 3). Additional color infor-

mation can break the degeneracy between atmosphere models. Thus adding XMM U data helps resolve this ambiguity. The best-fit models with the standard α enhancements select slightly sub-solar metallicity with a minimum $\chi^2/\text{DoF}=1.35$ for $(\log Z, \alpha) = (-1, 0.4)$. $(\log Z, \alpha) = (-0.5, 0.2)$ has an increased χ^2 ; however, the best fit model improves with the limited $(\log Z, \alpha) = (-0.5, 0)$ grid. The $(\log Z, \alpha) = (-0.5, 0)$ atmosphere represents the global best fit with $\Delta\chi^2 = -1$ improvement over $(\log Z, \alpha) = (-1, 0.4)$. Inspecting the synthesized colors, we note that the α changes between $(-0.5, 0)$ and $(-0.5, 0.2)$ introduce small $\sim 5\%$ differences in the emergent flux, especially in the bluest bands for $T < 7000$ K. Unfortunately, the online spectra have insufficient α coverage to fully explore this subtle effect.

The optical spectra of Romani et al. (2015) also probe the metallicity. In comparing Ca, Mg and Fe absorption line equivalent widths at maximum with BT-Settl model spectra, we see a best match to $\log Z = 0$, similar to the spider companions examined in Draghis et al. (2019). The discrepancy might be related to some imprecision in the colors synthesized from the spectra or in the optical broad band flux calibration. In Table 2, we show the estimated parameters of the Ug'r'i models using the $(\log Z, \alpha) = (-1, 0.4)$, $(-0.5, 0)$, and $(0, 0)$ atmospheres. Fig. 4 shows the best-fit light curve for the $(\log Z, \alpha) = (-0.5, 0)$ model.

The larger values of i now preferred imply a lower neutron star mass than found by KR20. To determine this mass (also shown in Table 2), we use the KR20 radial velocity measurement $K_c = 429.8 \pm 3.9$ km/s. Including 1σ statistical uncertainties, our mass estimates range from $M_{NS} = 1.85 - 2.3 M_\odot$, increasing with decreased metallicity. Although deprecated by the photometry, the spectroscopically preferred $\log Z = 0$ gives $1.91 \pm 0.06 M_\odot$ while the photometrically acceptable $\log Z = -1$ fit gives $M_{NS} = 2.18 \pm 0.10 M_\odot$. These are both well less than the $(\log Z = -1) M_{NS} = 2.24 \pm 0.09 M_\odot$ estimate of KR20.

4.2. X-ray Models

We model the X-ray emission with the IBS synchrotron emission prescription of Kandel et al. (2019) implemented in the ICARUS IBS code. The code discretizes the IBS (assumed to be thin) into triangular tiles of constant angular size as viewed from the pulsar, representing different zones from which synchrotron radiation is emitted. An electron and positron (hereafter e^\pm) population is injected into the IBS with energy spectrum in the flow frame

$$\dot{N}(\gamma_e)d\gamma_e = \dot{N}_0\gamma_e^{-p}d\gamma_e, \quad (2)$$

Parameters	-1.0/0.4	-0.5/0	0/0	KR20
i (deg)	$71.2^{+2.5}_{-2.0}$	$77.7^{+3.7}_{-2.7}$	$81.5^{+2.5}_{-2.9}$	$68.9^{+1.9}_{-1.8}$
M_{NS} (M_{\odot})	$2.18^{+0.10}_{-0.10}$	$1.98^{+0.09}_{-0.08}$	$1.91^{+0.07}_{-0.06}$	$2.24^{+0.09}_{-0.09}$
f_c	$0.93^{+0.01}_{-0.01}$	$0.91^{+0.01}_{-0.01}$	$0.90^{+0.007}_{-0.006}$	$0.94^{+0.01}_{-0.01}$
$L_{H,34}$	$2.51^{+0.10}_{-0.08}$	$2.51^{+0.09}_{-0.08}$	$2.48^{+0.06}_{-0.04}$	$2.6^{+0.1}_{-0.1}$
T_N (K)	5590^{+16}_{-17}	5630^{+15}_{-14}	5731^{+11}_{-11}	5682^{+14}_{-15}
d (kpc)	$3.33^{+0.04}_{-0.04}$	$3.29^{+0.04}_{-0.04}$	$3.34^{+0.03}_{-0.02}$	$3.30^{+0.04}_{-0.04}$
f_2 (μJy)	$1.7^{+0.2}_{-0.2}$	$1.6^{+0.2}_{-0.2}$	$1.8^{+0.2}_{-0.2}$	$1.2^{+0.2}_{-0.2}$
δm_r^{\dagger}	0.027(1)	0.035(1)	0.044(1)	0.031(1)
θ_{HS} (deg)	$339.3^{+4.8}_{-4.8}$	$322.6^{+5.9}_{-5.8}$	$302.2^{+3.9}_{-3.8}$	$324.0^{+10.1}_{-8.7}$
ϕ_{HS} (deg)	$72.2^{+5.1}_{-8.4}$	$73.4^{+4.2}_{-5.6}$	$78.9^{+2.1}_{-2.8}$	$73.2^{+5.0}_{-8.4}$
A_{HS}	$0.31^{+0.10}_{-0.07}$	$0.45^{+0.18}_{-0.13}$	$0.90^{+0.33}_{-0.29}$	$0.6^{+0.4}_{-0.2}$
r_{HS} (deg)	$20.8^{+2.6}_{-3.5}$	$16.9^{+3.2}_{-3.1}$	$17.0^{+2.1}_{-2.1}$	$15.5^{+3.9}_{-6.8}$
δm_U^{\dagger}	0.472(13)	0.477(13)	0.352(14)	–
χ^2/DoF	351/260	349/260	388/260	297/232

Table 2. Parameter results for optical modeling of WHT+OM J2215 data including the 68% confidence intervals. We show the best-fitting results with metallicities $(\log Z, \alpha) = (-1, 0.4)$, $(-0.5, 0)$, and $(0, 0)$. f_c is the Roche lobe filling factor, $L_{H,34}$ is the pulsar heating luminosity for an equatorially concentrated heating flux in units of 10^{34} erg s $^{-1}$, and d is the source distance. The hot spot coordinates (θ_{HS}, ϕ_{HS}) are defined so that $(0, 0)$ refers to the sub-pulsar point at the companion nose. The right column shows the fit results of KR20 which used $\log Z = -1$, assumed a different gravity darkening model, and did not have U data. \dagger δ are band offsets with last digit errors. δm_U is from the standard SAS flux calibration; however, we see evidence for a systematic calibration shift of ~ 0.5 mag. These fits assume $A_V = 0.40$, consistent with KR20, our X-ray fits and 3-D dust maps. We have conducted limited (expensive) tests with free A_V in fits, which shift the solutions to slightly larger A_V with higher L_H and T_N to correct the colors; other parameters remain within 1σ of the fixed A_V fit values.

Parameters	Fixed i	Free i
i (deg)	80	$51.8^{+16.9}_{-8.5}$
β	$2.29^{+0.24}_{-0.26}$	$1.52^{+0.51}_{-0.32}$
f_v	$6.4^{+5.8}_{-2.6}$	$3.4^{+3.2}_{-1.3}$
k	$0.076^{+0.028}_{-0.021}$	$0.208^{+0.150}_{-0.105}$
$\delta\Phi$	$0.026^{+0.008}_{-0.007}$	$0.032^{+0.010}_{-0.010}$
\dot{N}_0 (10^{31} s $^{-1}$)	$3.7^{+0.3}_{-0.6}$	$3.2^{+0.3}_{-0.4}$
F_b (10^{-14} erg cm $^{-2}$ s $^{-1}$)	$4.8^{+2.0}_{-1.4}$	$5.0^{+1.4}_{-1.4}$
\dot{M}_w (10^{-10} I_{45} M_{\odot} yr $^{-1}$)	$2.0^{+1.4}_{-1.0}$	$2.0^{+1.1}_{-0.9}$
χ^2/DoF	27/20	22/19

Table 3. Parameter results from IBS modeling of the X-ray light curve. \dot{M}_w is computed assuming $\dot{E} = 5.2 \times 10^{34}$ I_{45} erg s $^{-1}$ (Smith et al. 2023).

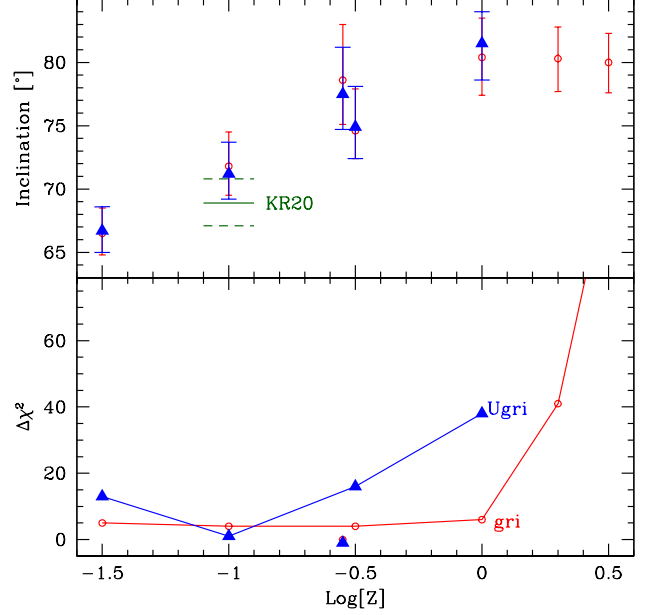


Figure 3. Sensitivity of the light curve fits to $\log Z$. The top panel shows the best-fit inclination, while the lower panel shows the $\Delta\chi^2$ from minimum. Fits of $g'r'i'$ alone are shown in red while fits of $Ug'r'i'$ are shown in blue. For $g'r'i'$ all $\log Z \leq 0$ metallicities are acceptable with near-identical χ^2 , leaving large i (and mass) uncertainty. Including XMM U breaks this degeneracy, preferring $\log Z = -1$ (the value used in KR20). The left points of the $\log Z = -0.5$ pair are for a lower $\alpha = 0$ element abundance; these represent the global minimum values found in the fits. See the text for details on α abundance.

where γ_e is the particle Lorentz factor in range $\gamma_{min} < \gamma_e < \gamma_{max}$, \dot{N}_0 (in e s $^{-1}$) is a global normalization coefficient related to the particle injection rate and p depends on the particle acceleration mechanism. After injection at a particular tile, the e^{\pm} population is advected to adjacent tiles with bulk Lorentz factor Γ_{bulk} . As the particles are advected, synchrotron losses cool the population. The residence time of the particle population in a particular zone is computed in the bulk flow frame as in Sullivan & Romani (2023). The synchrotron spectrum at each tile is calculated from the time-averaged particle spectrum in that tile. See Kandel et al. (2019) for further details on the emission prescription.

We assume an equatorially concentrated pulsar wind momentum flux $\propto \sin^2\theta_*$ in accordance with striped wind models (e.g. Michel 1973). θ_* denotes the angle between the pulsar spin axis (assumed to be aligned with the orbital angular momentum axis since spiders pulsars are strongly recycled) and a position in the wind. The pulsar wind collides with a spherical companion wind (Kandel et al. 2019). The stellar wind to pulsar wind momentum ratio $\beta = \dot{M}_w v_w c / \dot{E}_{PSR}$ (Romani

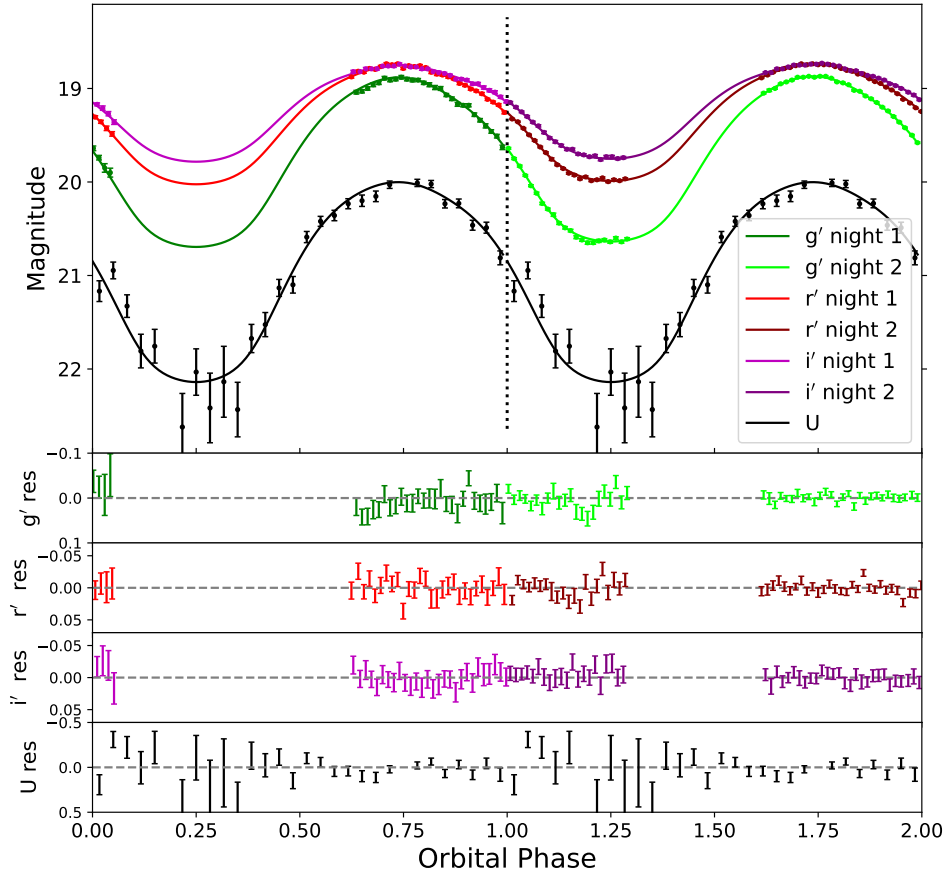


Figure 4. The best-fit companion optical light curve model plotted against the $g'r'i'$ data from WHT and the OM U data shifted by the estimated calibration offsets along with the residuals. The companion has $(\log Z, \alpha) = (-0.5, 0)$. Phase $0 \leq \Phi \leq 1$ shows WHT night 1 while $1 \leq \Phi \leq 2$ shows WHT night 2.

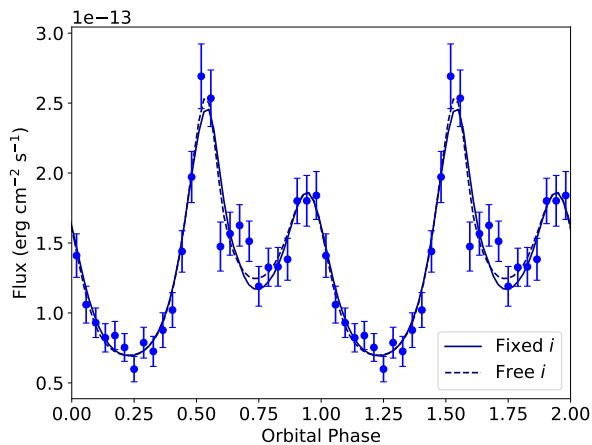


Figure 5. The best-fit IBS X-ray light curves. One model fit fixes $i = 80^\circ$, compatible with the optical modeling, while the other model fit leaves i as a free parameter.

& Sanchez 2016; Kandel et al. 2019) governs the overall shock geometry and sets the X-ray peak separation. The relative heights of the peaks are influenced by i as well as

the ratio of the stellar wind speed to the orbital speed $f_v = v_w/v_{orb}$. Low values of f_v cause the IBS shock structure to be swept back by the orbital motion, with the geometry tracing out an Archimedean spiral (see Romani & Sanchez (2016) for details on implementation in ICARUS), rather than a symmetric conical structure. The prescription for the bulk Lorentz factor in the post-shock flow is

$$\Gamma_{Bulk}(s) = \Gamma_{nose} \left(1 + k \frac{s}{r_0} \right), \quad (3)$$

where s is the arclength from the nose to a given point on the IBS, r_0 is the nose-standoff distance from the pulsar, Γ_{nose} is the bulk Lorentz factor at the nose, and k is a scaling parameter that controls the flow speed increase. The bulk flow direction is assumed to be parallel to the contact discontinuity.

We fit for β , f_v , and k . We perform fits with fixed $i = 80^\circ$, compatible with the best fitting $(\log Z, \alpha) = (-0.5, 0)$ optical model, and with i left as a free parameter. We fix $\Gamma_{nose} = 1.1$, consistent with numerical models (Bogovalov et al. 2008; Dubus et al.

2015; Kandel et al. 2019). At the IBS nose, we set $B_{IBS} = 3B_{LC} (R_{LC}/r_0) \approx 70$ G (where B_{LC} is the magnetic field at the light cylinder radius R_{LC} ; the factor of 3 is due to relativistic shock compression; Sullivan & Romani 2023), based on the inferred orbital separation $a \approx 1.5 \times 10^{11}$ cm, $P_s = 2.61$ ms and $\dot{P}_s = 2.38 \times 10^{-20}$ (Smith et al. 2023). We set $p = 0.76$ so that our IBS model spectrum has $\Gamma_{IBS} = 0.94$ in the 0.5 – 10 keV band, consistent with the actual spectral results shown in Table 1. Our fits prefer a forward phase shift $\delta\Phi \sim 0.03$ from the radio/gamma-ray determined ephemeris and from our optical phase. We leave $\delta\Phi$ as a fit parameter. We also fit the injected particle spectrum normalization \dot{N}_0 and a phase independent flux F_b added as an offset. We add the offset to account for additional X-ray flux present in the source, possibly due to a pulsar wind nebula (PWN) or the magnetosphere; this component is also present in the spectral fits, as noted above.

Our best-fit light curves are shown in Fig. 5 and the parameter estimates are shown in Table 3. Our model fits the data moderately well, with $\chi^2/\text{DoF} = 1.35$ when fixing i and $\chi^2/\text{DoF} = 1.16$ when leaving i free. This corresponds to an Akaike information criterion (AIC) value of 39 for the fixed i model and 36 for the free i model. Departures from a simple light curve in the phase range $\Phi = 0.6 - 0.7$ contribute a large factor to the χ^2 . In examining the orbit-to-orbit variations, we find that this phase range has somewhat higher variability than the rest of the light curve, but we are unable to attribute the structure in this phase range to IBS flares (as have been seen in other spider pulsars; e.g. An et al. 2017). Thus, the flux dip at $\Phi \approx 0.6$ might represent an absorption component, or, alternatively, the flux increase at $\Phi \approx 0.65$ might represent an extra emission component, possibly structure in a thick post-shock flow not captured by our thin-shock geometry. We have left these points in the fit to be conservative; excising these points barely changes the fixed i best-fit parameters. We also note the low bin at $\Phi = 0.25$. While at the appropriate phase for a companion eclipse, its significance is low. Furthermore, we would not expect significant occultation of the extended IBS at $i \lesssim 85^\circ$.

The model fitting gives values $\beta \approx 2$ and $f_v \approx 3 - 6$, signaling a rather flat IBS and slow companion wind. If left free, i decreases to 52_{-9}^{+17} deg to accommodate the bridge flux (including the $\Phi \approx 0.65$ component). Such low i implies $M_{NS} = 3.8_{-1.4}^{+3.9} M_\odot$; the central value is unphysical, although less than 2σ different from our optical mass determinations. Indeed, i itself is only in $\sim 1.5\sigma$ disagreement with the possible optical values. We thus consider the fixed i IBS fit more reliable.

5. DISCUSSION AND CONCLUSION

Our optical and X-ray model fits, while imperfect, provide more realistic estimates of the parameters of J2215. Having used the radial velocity K_c from Kandel & Romani (2020), we believe that these new values should supersede the results of that paper and those in the less physical modeling of Linares et al. (2018), especially given the unusual sensitivity to the metallicity. Our best-fit $(\log Z, \alpha) = (-0.5, 0)$ result $M_{NS} = 1.98 \pm 0.08 M_\odot$ is more than 2σ less than the KR20 estimate. If we adopt $\log Z = 0$, as suggested by the optical spectroscopy, the mass lowers by an additional $\sim 1\sigma$ to $M_{NS} = 1.91 \pm 0.06 M_\odot$. Overall, including the metallicity-induced systematic uncertainty, masses from $\approx 1.85 - 2.3 M_\odot$ remain acceptable. Improved absolute photometry, especially in UV bands could help break the metallicity degeneracy. Our present result does not strongly constrain the dense matter equation of state given these uncertainties, but can still be valuable for high mass neutron star population studies (e.g. Brandes et al. 2023; Komoltsev et al. 2024).

With well-detected light curve peaks, our X-ray results are much more robust than those of Romani & Sanchez (2016). Our modeling suggests $\beta \lesssim 2.5$ and $f_v < 10$. From these results and $\dot{E} = 5.2 \times 10^{34}$ erg s⁻¹ (Smith et al. 2023), we estimate the companion mass-loss rate

$$\dot{M}_w = \frac{\beta \dot{E}}{f_v v_{orb} c}, \quad (4)$$

showing the results in Table 3. $\dot{M}_w \approx 2 \times 10^{-10} I_{45} M_\odot \text{ yr}^{-1}$ suggests that the companion should evaporate in $\sim 1.5/I_{45}$ Gyr, a modest fraction of the age of the universe, and comparable to the $\tau_c = 1.2$ Gyr characteristic spindown age. This is short enough for J2215 to evolve into an isolated MSP (Kluźniak et al. 1988). However, with β unusually close to unity, the IBS location and thus mass-loss rate are sensitive to the fit details; these include the small unexplained phase shift.

The estimated value of the phase-independent flux from the light curve fits $F_b \approx 5 \times 10^{-14}$ erg cm⁻² s⁻¹ is in good agreement with the phase-independent flux estimated from the spectral fitting F_0 . These fluxes correspond to a luminosity of 7×10^{31} erg s⁻¹ at $d = 3.3$ kpc and could originate from magnetospheric emission or, more likely, from a faint, compact PWN (e.g. Li et al. 2008). The spectral index $\Gamma_0 \approx 1.5$ is quite consistent with a PWN source, while the efficiency $L \approx 10^{-3} \dot{E}$ is similar to that of other observed PWNe. The slightly larger value of F_0 would include a small amount of emission from the wings of the IBS peaks in the off-phase.

It is also useful to compare our measured energy fluxes with the pulsar spin-down power budget $\dot{E} = 5 \times 10^{34}$

$I_{45} \text{ erg s}^{-1}$. Several neutron star masses have been securely measured above $2 M_{\odot}$, pointing towards a quite stiff equation of state. We can estimate $I_{45} \approx [0.8 - 1.2](M/M_{\odot})^{3/2}$ (Lattimer & Schutz 2005), i.e. $2.2 - 3.4$ for $2 M_{\odot}$. The $\sin^2\theta_*$ -distributed heating luminosity $L_H \approx 2.5 \times 10^{34} \text{ erg s}^{-1}$ is in good accord with the isotropic GeV gamma-ray luminosity measured by the *Fermi* LAT, $L_{\gamma} = 3.3 \times 10^{34} \text{ erg s}^{-1}$, suggesting that our ‘direct heating’ is dominated by the GeV photons. This requires that the radiation be directed toward the companion at the pulsar spin equator, as expected from outer magnetosphere/wind emission models (e.g. Philippov & Spitkovsky 2018) for spin-orbit aligned recycled pulsars. This gamma-ray direct heating power is a substantial fraction of the spin-down energy budget, but can be comfortably accommodated for $I_{45} = 2 - 3$. This also reduces our estimated evaporation timescale below 1 Gyr.

Our IBS fit also estimates the e^{\pm}/B pulsar wind power \dot{E}_{pw} , which is processed by the shock into a power-law electron distribution,

$$\dot{E}_{pw} = \frac{\dot{N}_0}{2-p} m_e c^2 (\gamma_{\max}^{2-p} - \gamma_{\min}^{2-p}). \quad (5)$$

The observed 0.5-10 keV X-ray spectrum comes from $10^4 < \gamma < 10^5$ e^{\pm} particles. Our fit $\dot{N}_0 \sim 3 - 4 \times 10^{31} \text{ s}^{-1}$ thus gives a minimum $\dot{E}_{pw} \gtrsim 5 \times 10^{31} \text{ erg s}^{-1}$ for $p \approx 0.8$. This is well below the available power $\dot{E} - L_H \approx 12 \times 10^{34} \text{ erg s}^{-1}$ for $I_{45} \approx 3$. To avoid saturating the residual spin-down power, there is an upper limit of $\gamma_{\max} \sim 5.5 \times 10^7$. Higher energy X-ray and gamma-ray measurements can further probe the high γ e^{\pm} population (which cools rapidly). If magnetic reconnection is the primary acceleration mechanism (as suggested by the very hard observed spectra), the maximum electron energy should be $\gamma_{\max} \sim \sigma \gamma_{\min}$, where $\sigma = B^2/(4\pi\gamma_{\min}n_0m_e c^2)$ is the pulsar wind magnetization and n_0 is the e^{\pm} number density (Sironi & Spitkovsky 2011, 2014). As expected, the J2215 pulsar wind should be very strongly magnetized with $10 \lesssim \sigma \lesssim 6 \times 10^7$. Finally, the companion hot spot indi-

cates extra localized heating. Sanchez & Romani (2017) attribute companion hot spots to IBS-energized particles precipitating to the companion magnetic poles. In our fits, the small β allows the relatively flat IBS shock to capture $\sim 40 - 50\%$ of the \dot{E}_{pw} flux, while the thermal emission of the hot spot represents $1 \times 10^{32} \text{ erg s}^{-1}$. Only a small fraction $\sim 2 \times 10^{-3}$ of the maximum available IBS-processed pulsar wind power needs to reach the surface to heat the companion magnetic pole. Simultaneous optical/UV observations would be useful to re-check the U band normalization and further constrain the hot spot contribution and atmosphere metallicity.

J2215’s high inferred mass-loss rate makes this system a plausible isolated MSP progenitor, while its unusually flat IBS may reprocess a large fraction of the spin-down power. The hard X-ray spectrum and sharp peaks provide an important probe of relativistic shock dynamics and particle acceleration. Higher energy observations (e.g. with NuSTAR) should further constrain the IBS e^{\pm} population. Since the prominent IBS peaks indicate beamed emission and thus moderate bulk Lorentz factors in the IBS flow, the various orbital phases probe different portions of the shock with varying obliquity. Thus, IBS-dominated spider pulsars, like J2215, show emission from a range of relativistic shock geometries. Future phase-resolved spectrum and polarization measurements of these natural laboratories can be compared with numerical simulations to advance our understanding of oblique, strongly magnetized relativistic shocks.

ACKNOWLEDGEMENTS

The authors thank Dinesh Kandel for help using ICARUS and for clarifications on the previous optical modeling as well as the anonymous referee for helpful feedback. This work was supported in part by NASA grant 80NSSC22K1506. A.S. acknowledges the support of the Stanford University Physics Department Fellowship and the National Science Foundation Graduate Research Fellowship.

REFERENCES

- Allard, F. 2014, in *Exploring the Formation and Evolution of Planetary Systems*, ed. M. Booth, B. C. Matthews, & J. R. Graham, Vol. 299, 271–272, doi: [10.1017/S1743921313008545](https://doi.org/10.1017/S1743921313008545)
- An, H., Romani, R. W., Johnson, T., Kerr, M., & Clark, C. J. 2017, *ApJ*, 850, 100, doi: [10.3847/1538-4357/aa947f](https://doi.org/10.3847/1538-4357/aa947f)
- Anders, E., & Grevesse, N. 1989, *GeoCoA*, 53, 197, doi: [10.1016/0016-7037\(89\)90286-X](https://doi.org/10.1016/0016-7037(89)90286-X)
- Atwood, W. B., Abdo, A. A., Ackermann, M., et al. 2009, *ApJ*, 697, 1071, doi: [10.1088/0004-637X/697/2/1071](https://doi.org/10.1088/0004-637X/697/2/1071)
- Balucinska-Church, M., & McCammon, D. 1992, *ApJ*, 400, 699, doi: [10.1086/172032](https://doi.org/10.1086/172032)

- Bogovalov, S. V., Khangulyan, D. V., Koldoba, A. V., Ustyugova, G. V., & Aharonian, F. A. 2008, *MNRAS*, 387, 63, doi: [10.1111/j.1365-2966.2008.13226.x](https://doi.org/10.1111/j.1365-2966.2008.13226.x)
- Brandes, L., Weise, W., & Kaiser, N. 2023, *PhRvD*, 108, 094014, doi: [10.1103/PhysRevD.108.094014](https://doi.org/10.1103/PhysRevD.108.094014)
- Breton, R. P., van Kerkwijk, M. H., Roberts, M. S. E., et al. 2013, *ApJ*, 769, 108, doi: [10.1088/0004-637X/769/2/108](https://doi.org/10.1088/0004-637X/769/2/108)
- Broderick, J. W., Fender, R. P., Breton, R. P., et al. 2016, *MNRAS*, 459, 2681, doi: [10.1093/mnras/stw794](https://doi.org/10.1093/mnras/stw794)
- Buchner, J., Georgakakis, A., Nandra, K., et al. 2014, *A&A*, 564, A125, doi: [10.1051/0004-6361/201322971](https://doi.org/10.1051/0004-6361/201322971)
- Claret, A., & Bloemen, S. 2011, *A&A*, 529, A75, doi: [10.1051/0004-6361/201116451](https://doi.org/10.1051/0004-6361/201116451)
- Doe, S., Nguyen, D., Stawarz, C., et al. 2007, in *Astronomical Society of the Pacific Conference Series*, Vol. 376, *Astronomical Data Analysis Software and Systems XVI*, ed. R. A. Shaw, F. Hill, & D. J. Bell, 543
- Draghis, P., Romani, R. W., Filippenko, A. V., et al. 2019, *ApJ*, 883, 108, doi: [10.3847/1538-4357/ab378b](https://doi.org/10.3847/1538-4357/ab378b)
- Dubus, G., Lamberts, A., & Fromang, S. 2015, *A&A*, 581, A27, doi: [10.1051/0004-6361/201425394](https://doi.org/10.1051/0004-6361/201425394)
- Feroz, F., & Hobson, M. P. 2008, *MNRAS*, 384, 449, doi: [10.1111/j.1365-2966.2007.12353.x](https://doi.org/10.1111/j.1365-2966.2007.12353.x)
- Feroz, F., Hobson, M. P., & Bridges, M. 2009, *MNRAS*, 398, 1601, doi: [10.1111/j.1365-2966.2009.14548.x](https://doi.org/10.1111/j.1365-2966.2009.14548.x)
- Feroz, F., Hobson, M. P., Cameron, E., & Pettitt, A. N. 2019, *The Open Journal of Astrophysics*, 2, 10, doi: [10.21105/astro.1306.2144](https://doi.org/10.21105/astro.1306.2144)
- Freeman, P., Doe, S., & Siemiginowska, A. 2001, in *Society of Photo-Optical Instrumentation Engineers (SPIE) Conference Series*, Vol. 4477, *Astronomical Data Analysis*, ed. J.-L. Starck & F. D. Murtagh, 76–87, doi: [10.1117/12.447161](https://doi.org/10.1117/12.447161)
- Gentile, P. A., Roberts, M. S. E., McLaughlin, M. A., et al. 2014, *ApJ*, 783, 69, doi: [10.1088/0004-637X/783/2/69](https://doi.org/10.1088/0004-637X/783/2/69)
- Green, G. M., Schlafly, E. F., Finkbeiner, D., et al. 2018, *MNRAS*, 478, 651, doi: [10.1093/mnras/sty1008](https://doi.org/10.1093/mnras/sty1008)
- Hessels, J. W. T., Roberts, M. S. E., McLaughlin, M. A., et al. 2011, in *American Institute of Physics Conference Series*, Vol. 1357, *Radio Pulsars: An Astrophysical Key to Unlock the Secrets of the Universe*, ed. M. Burgay, N. D’Amico, P. Esposito, A. Pellizzoni, & A. Possenti, 40–43, doi: [10.1063/1.3615072](https://doi.org/10.1063/1.3615072)
- Hui, C. Y., & Li, K. L. 2019, *Galaxies*, 7, 93, doi: [10.3390/galaxies7040093](https://doi.org/10.3390/galaxies7040093)
- Jansen, F., Lumb, D., Altieri, B., et al. 2001, *A&A*, 365, L1, doi: [10.1051/0004-6361:20000036](https://doi.org/10.1051/0004-6361:20000036)
- Kandel, D., & Romani, R. W. 2020, *ApJ*, 892, 101, doi: [10.3847/1538-4357/ab7b62](https://doi.org/10.3847/1538-4357/ab7b62)
- . 2023, *ApJ*, 942, 6, doi: [10.3847/1538-4357/aca524](https://doi.org/10.3847/1538-4357/aca524)
- Kandel, D., Romani, R. W., & An, H. 2019, *ApJ*, 879, 73, doi: [10.3847/1538-4357/ab24d9](https://doi.org/10.3847/1538-4357/ab24d9)
- . 2021, *ApJL*, 917, L13, doi: [10.3847/2041-8213/ac15f7](https://doi.org/10.3847/2041-8213/ac15f7)
- Kluzniak, W., Ruderman, M., Shaham, J., & Tavani, M. 1988, *Nature*, 334, 225, doi: [10.1038/334225a0](https://doi.org/10.1038/334225a0)
- Komoltsev, O., Somasundaram, R., Gorda, T., et al. 2024, *PhRvD*, 109, 094030, doi: [10.1103/PhysRevD.109.094030](https://doi.org/10.1103/PhysRevD.109.094030)
- Lattimer, J. M., & Prakash, M. 2007, *PhR*, 442, 109, doi: [10.1016/j.physrep.2007.02.003](https://doi.org/10.1016/j.physrep.2007.02.003)
- Lattimer, J. M., & Schutz, B. F. 2005, *ApJ*, 629, 979, doi: [10.1086/431543](https://doi.org/10.1086/431543)
- Li, X.-H., Lu, F.-J., & Li, Z. 2008, *ApJ*, 682, 1166, doi: [10.1086/589495](https://doi.org/10.1086/589495)
- Linares, M. 2014, *ApJ*, 795, 72, doi: [10.1088/0004-637X/795/1/72](https://doi.org/10.1088/0004-637X/795/1/72)
- Linares, M., Shahbaz, T., & Casares, J. 2018, *ApJ*, 859, 54, doi: [10.3847/1538-4357/aabde6](https://doi.org/10.3847/1538-4357/aabde6)
- Michel, F. C. 1973, *ApJL*, 180, L133, doi: [10.1086/181169](https://doi.org/10.1086/181169)
- Philippov, A. A., & Spitkovsky, A. 2018, *ApJ*, 855, 94, doi: [10.3847/1538-4357/aaabbc](https://doi.org/10.3847/1538-4357/aaabbc)
- Ray, P. S., Abdo, A. A., Parent, D., et al. 2012, *arXiv e-prints*, arXiv:1205.3089, doi: [10.48550/arXiv.1205.3089](https://doi.org/10.48550/arXiv.1205.3089)
- Roberts, M. S. E. 2013, in *Neutron Stars and Pulsars: Challenges and Opportunities after 80 years*, ed. J. van Leeuwen, Vol. 291, 127–132, doi: [10.1017/S174392131202337X](https://doi.org/10.1017/S174392131202337X)
- Romani, R. W., Graham, M. L., Filippenko, A. V., & Kerr, M. 2015, *ApJL*, 809, L10, doi: [10.1088/2041-8205/809/1/L10](https://doi.org/10.1088/2041-8205/809/1/L10)
- Romani, R. W., & Sanchez, N. 2016, *ApJ*, 828, 7, doi: [10.3847/0004-637X/828/1/7](https://doi.org/10.3847/0004-637X/828/1/7)
- Sanchez, N., & Romani, R. W. 2017, *ApJ*, 845, 42, doi: [10.3847/1538-4357/aa7a02](https://doi.org/10.3847/1538-4357/aa7a02)
- Schroeder, J., & Halpern, J. 2014, *ApJ*, 793, 78, doi: [10.1088/0004-637X/793/2/78](https://doi.org/10.1088/0004-637X/793/2/78)
- Sironi, L., & Spitkovsky, A. 2011, *ApJ*, 741, 39, doi: [10.1088/0004-637X/741/1/39](https://doi.org/10.1088/0004-637X/741/1/39)
- . 2014, *ApJL*, 783, L21, doi: [10.1088/2041-8205/783/1/L21](https://doi.org/10.1088/2041-8205/783/1/L21)
- Smith, D. A., Abdollahi, S., Ajello, M., et al. 2023, *ApJ*, 958, 191, doi: [10.3847/1538-4357/acee67](https://doi.org/10.3847/1538-4357/acee67)
- Steiner, A. W., Lattimer, J. M., & Brown, E. F. 2013, *ApJL*, 765, L5, doi: [10.1088/2041-8205/765/1/L5](https://doi.org/10.1088/2041-8205/765/1/L5)
- Sullivan, A. G., & Romani, R. W. 2023, *ApJ*, 959, 81, doi: [10.3847/1538-4357/ad09ae](https://doi.org/10.3847/1538-4357/ad09ae)
- van Paradijs, J., Allington-Smith, J., Callanan, P., et al. 1988, *Nature*, 334, 684, doi: [10.1038/334684a0](https://doi.org/10.1038/334684a0)
- Wadiasingh, Z., Harding, A. K., Venter, C., Böttcher, M., & Baring, M. G. 2017, *ApJ*, 839, 80, doi: [10.3847/1538-4357/aa69bf](https://doi.org/10.3847/1538-4357/aa69bf)

Yao, J. M., Manchester, R. N., & Wang, N. 2017, *ApJ*, 835,
29, doi: [10.3847/1538-4357/835/1/29](https://doi.org/10.3847/1538-4357/835/1/29)